Available online at www.sciencedirect.com

SciVerse ScienceDirect

Ceramics International 38 (2012) 4943–4951

CERAMICS INTERNATIONAL

www.elsevier.com/locate/ceramint

# Synthesis and characterization of neodymium doped ceria nanocrystalline ceramic structures

İbrahim Uslu [a], Arda Aytimur [a,*], Mustafa Kemal Öztürk [b], Serhat Koçyiğit [a]

[a] Gazi University, Gazi Faculty of Education, Teknikokullar, Ankara 06500, Turkey
[b] Gazi University, Faculty of Science, Teknikokullar, Ankara 06500, Turkey

Received 12 February 2012; received in revised form 20 February 2012; accepted 27 February 2012
Available online 5 March 2012

**Abstract**

In this study, a new method to synthesize neodymium doped ceria ceramic nanopowders by the electrospinning of the hybrid polymers solution of their composite precursor was put forward. Calcined and sintered nanopowders were characterized by FT-IR, XRD, BET, SEM, and AFM techniques. According to the XRD analysis, the obtained powders are single phase and independent of the dopant concentration in the range investigated. The crystallite sizes were calculated using Scherrer equation. Moreover, lattice parameters, dislocation densities and microstrain values were calculated. BET results show that the increase of the neodymium doped content decrease the surface area of the composite powders, confirming the highly ordered micro and mesostructure. SEM and AFM results show that the samples have spherical grains. According to the surface roughness measurements, the increase in the amount of neodymium and the decrease in the amount of cerium decreased the surface roughness.



*Keywords:* A. Calcination; A. Precursors: organic; A. Sintering; B. Nanocomposites; D. $CeO_2$; D. Transition metal oxides

## 1. Introduction

An important property required regarding the electrolyte of solid oxide fuel cells (SOFC) is them having high oxygen-ion conductivity [1].

There are two possibilities to enhance the oxygen-ion conductivity of the ceria ($CeO_2$) itself, either by the promotion of $Ce^{4+}$ reduction into $Ce^{3+}$ or by chemically doping the ceria with other transition or rare-earth elements. Rare earth doped ceria, which has higher oxygen ion conductivity than yttria-stabilized zirconia is currently attracting much attention because it is seen as a candidate material for serving as the solid electrolyte of SOFC [2–9].

The choice of dopant elements, their introduced amounts, and the preparation method of the composite matrix also has a very strong influence on the homogeneity and the stability of the solid solutions. A recent study [10] on the oxygen diffusion of cerium oxide doped with neodymium (Nd) demonstrated that its oxygen diffusion coefficient is larger than that of cerium oxide doped with gadolinium (Gd) and many other rare earth elements at a similar concentration of additives.

There are some results available on the oxygen ion conductivity of the rare earth doped ceria in the literature [11–15].

Especially Faber et al., Ifan et al., and Aneflous et al. characterized the ionic conductivity of a series of neodymia doped ceria solid solutions. They have concluded that these ceramic crystalline materials exhibit conductivity levels of up to an order of magnitude higher than yttria stabilized zirconia.

In this paper, we report the synthesis of nanocrystalline Nd-doped ceria by the calcination and sintering of the electrospun fibers of the polyvinyl alcohol (PVA)/Ce–Nd acetate polymer composite solution.

The nanocrystalline ceramics have far superior powder properties. First of all, they have large surface areas, high sinterability, etc. [16]. Also their optical, electronic catalytic [17] and magnetic [18] properties are better than their microcrystalline structures.

As far as we are aware of, there is no reported literature available on another study of the preparation and characterization

* Corresponding author. Tel.: +90 312 202 8017; fax: +90 312 202 8041.
*E-mail address:* ardaaytimur@hotmail.com (A. Aytimur).

0272-8842/$36.00 
doi:10.1016/j.ceramint.2012.02.087

of nanocrystalline Nd doped ceria using the electrospinning technique which is an inexpensive method to generate inorganic nanofiber structures.

## 2. Materials and methods

In the experiments, the PVA (average molecular weight of 85,000–124,000, Sigma Aldrich), the cerium (III) acetate (Sigma Aldrich), and the neodymium (III) acetate (Sigma Aldrich) were used. Acetic acid (Merck) and ultrapure deionized water were used as solvents.

The experiments were carried out in three major stages: (i) the preparation of the metal acetate composite precursor hybrid polymeric (PVA) solution, (ii) the electrospinning of the composite precursor polymeric solution to generate composite nanofibers consisting of matrix polymer and precursor (neodymium acetate, cerium acetate and PVA) at the room temperature, and (iii) the calcination or the chemical conversion of the precursor polymeric nanofibers into the desired ceramic nanopowder at an elevated temperature, with the concomitant removal of all the hybrid PVA polymer solutions from the precursor at 850 °C. The heating and cooling rates were fixed at 8 °C/min.

The aqueous PVA solution (10%) was first prepared by dissolving the PVA powder in ultra pure distilled water and heating it to 90 °C, stirring it for 3 h, and then, cooling it down to room temperature while continuously stirring it for two more hours. In the experiments, two hybrid polymer solutions were separately prepared and compared in order to see the effect of Ce and Nd on the calcination behavior and to provide further opportunity to explore possible compositional dependence of the micro-structure.

For the first solution (solution 1), 0.1 g of the neodymium (III) acetate and 0.9 g of the cerium (III) acetate powders were dissolved in the 4 g deionized water and 16 g acetic acid solution. After stirring at room temperature for more than an hour, the resulting solution was added drop by drop to the 50 g aqueous PVA (10% w/w) solution. The hybrid polymer solution was further stirred for 6 h. For the second solution (solution 2), 0.3 g of the neodymium (III) acetate and 0.7 g of the cerium (III) acetate powders were dissolved in 4 g deionized water and 16 g acetic acid solution. After stirring at room temperature for more than an hour, the resulting solution was added drop by drop to the 50 g aqueous PVA (10%, w/w) solution.

As a final product, the viscous gels of the PVA/Nd–Ce acetate hybrid polymer solutions were prepared.

For the electrospinning experiments, the PVA/(Nd–Ce) acetate hybrid polymer solutions were placed in a 10 ml plastic syringe and connected to a high-voltage generator to generate positive DC voltages. The solutions were delivered to the needle by a syringe pump with a flow rate of 0.8 ml/h (New Era Pump Systems Inc., USA). The distance between the capillary tip and the alumina-coated collector was fixed at 18 cm. The voltage was 20 kV during the experiments. A grounded iron drum, covered with an aluminum foil, served as the counter electrode. Free nanofiber mats were obtained by peeling off the aluminum foil. Nanofiber mats were calcined at 850 °C at atmospheric conditions for 2 h in a tubular furnace and sintered again at the same heating conditions.

The pH and the electrical conductivity of the solutions were measured using the Wissenschaftlich–Technische–Werkstätten WTW and 315i/SET apparatus. The viscosity values of the hybrid polymer solutions were measured using an AND SV-10 viscometer. The surface tension values of the complex hybrid polymer solutions were measured using a KRUSS model manual measuring system.

The Fourier Transformations Infrared Spectroscopy (FT-IR) results were obtained using a Thermo Nicolette 6700 spectrophotometer with ATR module. The composite morphology was observed using the scanning electron microscopy technique. The JEOL JSM 6060 was used on the samples sputtered with gold and observed at an accelerating voltage of 10 kV. The particle diameters were measured using the image processing software, ImageJ (Image Pro-Express, Version 5.0.1.26, Media Cybernetics Inc.) which is a public domain Java image processing program [19].

The crystal structures of the calcined powders were investigated by means of X-ray diffraction using an XRD Bruker AXS D8 Advance diffractometer with the Vario1 Johansson focusing monochromator Cu K$\alpha$1 radiation. The surface areas were determined using nitrogen adsorption isotherms at −196 °C on a Micromeritics Gemini V2380 surface area analyzer system. The samples were prepared for measurement by degassing them at 150 °C for 24 h. Surface areas were calculated using the BET (Brunauer–Emmett–Teller) method and the pore size distributions were determined using the BJH (Barrett–Joyner–Halenda) method on the adsorption branch of the hysteresis curve.

The surface morphology of the obtained nanocrystalline powder samples was taken as an image by scanning an area of $1 \times 1$ μm using an AFM (Atomic Force Microscope, Nanosurf easyScan 2, Switzerland). Nanosurface roughness measurements were completed using an atomic force microscope and the Nanosurf easyScan 2 software. Commercially available AFM tips (detector side Al coating, thickness of the tip was 7 μm, tip lenght was 225 μm, tip width was 38 μm with a 48 N/m force constant and 190 kHz resonance frequency) were used in intermittent contact (also called tapping) mode.

## 3. Results and discussion

The pH, viscosity, electrical conductivity and the surface tension of the polymer solutions before the electrospinning experiment were measured and are given in Table 1. The addition of Nd acetate as the doping material decreased the electrical conductivity, pH, viscosity and the surface tension of the hybrid polymer solution.

The FT-IR spectra were recorded at the room temperature in a spectral range of 4000–600 $cm^{-1}$. To characterize the polymer hybrid solution to the nanocrystal ceramic conversion, the precursor PVA hybrid polymer nanofibers, the calcined and the sintered powders were characterized by the FTIR. Fig. 1 shows the FTIR spectra of the PVA nanofibers and the sintered powders of sample 1. In the PVA spectrum, the IR bands related

Table 1
Physical properties of the polymer solutions.

| Polymer solution | Conductivity (μS/cm) | Viscosity (Pa s) | pH | Surface tension (mN/m) |
|---|---|---|---|---|
| Solution 1 | 2530 | 391 | 3.09 | 46 |
| Solution 2 | 2420 | 333 | 3.07 | 45 |

to its polymeric structure can be seen. The strongest band at 2920 $cm^{-1}$ is related to CH and $CH_2$ stretches, and the weakest band at 1730 $cm^{-1}$ is related to C=O stretching of the residual acetate group [20].

The calcined powder exhibits bands related to the presence of carbonaceous materials (at 1580–1300 $cm^{-1}$). In the FT-IR spectra of the calcined samples, the disappearance of the bands due to CH and $CH_2$ stretches was the result of the degradation of the PVA and acetate structures. After sintering the calcined samples, the bands in the frequency region from 1200 to 1300 $cm^{-1}$ were assigned to some traces of undecomposed carbonaceous materials in the calcined powders and disappeared following the sintering process. It is well known that the broad absorption band located in the area from 3200 to 3600 $cm^{-1}$ approximately corresponds to the –OH stretching vibration. In addition, due to the stretching frequency of Ce–O a new band can be seen below 760 $cm^{-1}$ [21].

The XRD curves of Nd doped ceria electrospun nanofibers and nanocrystalline powders obtained from calcined and sintered samples of both solutions 1 and 2 are shown in Figs. 2 and 3, respectively.

From Fig. 2, it is seen that the XRD pattern of the fibers show amorphous structure and confirms that neither PVA nor Nd doped Ceria crystallize measurably in the as-spun fiber. The observed reflections at the d-spacings (Å) of 3.14, 2.71, 1.92, 1.63, and 1.57 for the fiber samples correspond well to the (1 1 1), (2 0 0), (2 2 0), (3 1 1) and (2 2 2) reflections, respectively. The same crystalline structure was observed both

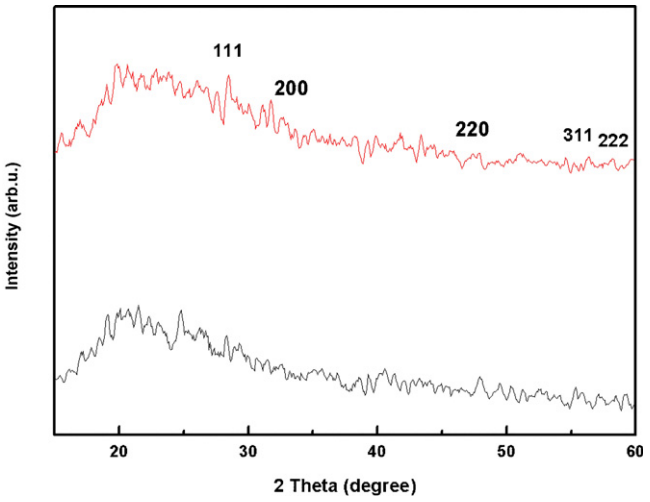


Fig. 2. X-ray diffraction patterns of the nanofibers obtained from: (a) solution-1, and (b) solution-2.

for the calcined and for the sintered samples given in Fig. 3(a–d). All of the peaks can be indexed to a pure cubic fluorite structure of $CeO_2$ (space group: Fm3m) which is in agreement with the JCPDS file for $CeO_2$ (JCPDS 028-0266). $2\theta$ values of 28.309°, 32.791°, 47.046°, 47.596°, 55.825° and 58.540° according to the JCP2 028-0266 card number is in good agreement with Fig. 3(a–d). It is worth noting that the overwhelmingly intensive diffraction peak is located at $2\theta = 28.40°$, which is from the [1 1 1] lattice plane of the fcc $CeO_2$ [22].

According to the XRD analysis, the obtained powders are single phase and independent of the dopant concentration in the range investigated. After sintering the calcined powders at 850 °C for an hour, the XRD peaks became sharper indicating that the crystallinity of Nd doped $CeO_2$ is accelerated by the sintering process (Fig. 3(b and d)).

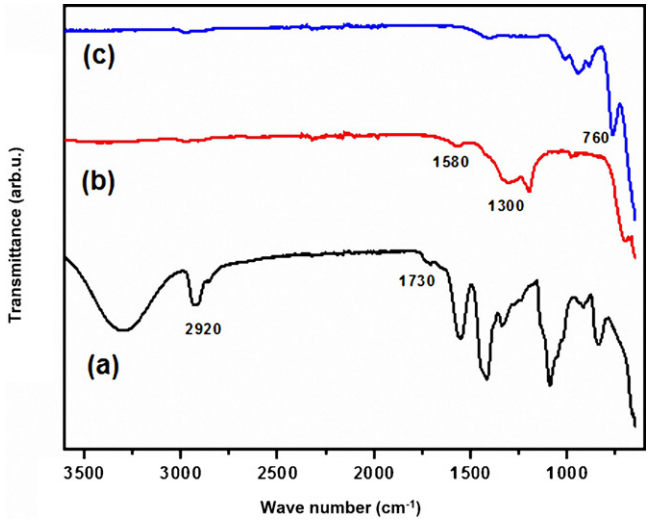


Fig. 1. FTIR spectra of Nd doped ceria of (a) polymer nanofibers, (b) after calcination of the powder samples, and (c) after sintering of the calcined powder samples.

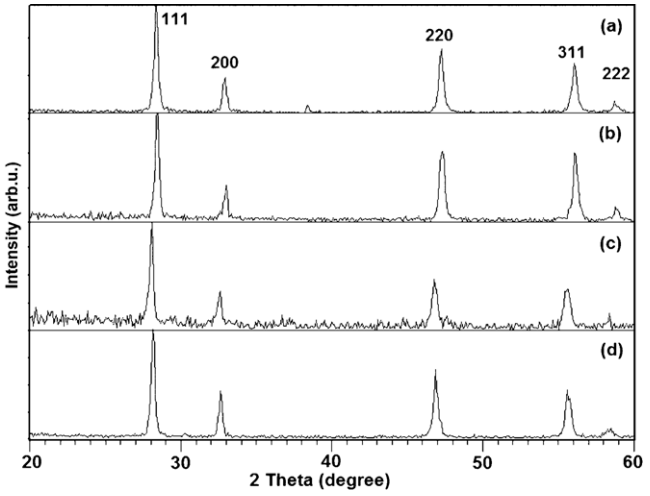


Fig. 3. XRD curves of Nd doped ceria nanocrystalline powders obtained from: (a) after calcination solution 1 at 850 °C, (b) after sintering of the calcined sample of solution-1, (c) after calcination solution 2 at 850 °C, and (d) after sintering of the calcined sample of solution-2.

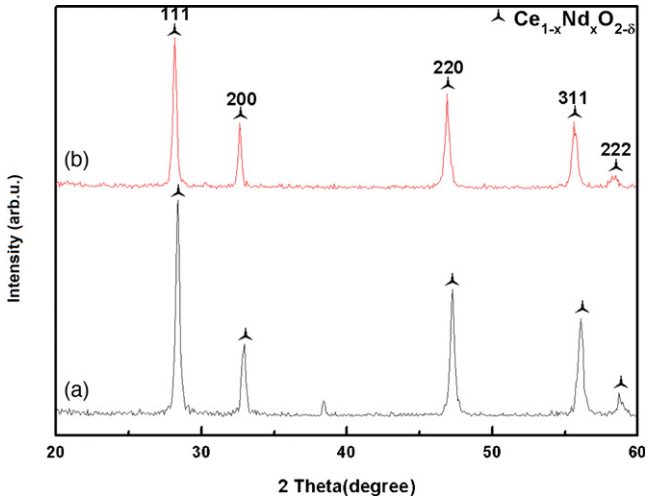


Fig. 4. XRD curves of Nd doped ceria powders obtained from: (a) after sintering of the calcined powder sample of solution-1, and (b) after sintering of the calcined powder sample of solution-2.

As it can be seen in Fig. 4, sintering the samples after the calcination caused the decrease of the width of the diffraction peaks for Nd doped ceria with respect only to the calcined samples. The dissolution of the $Nd_2O_3$ in a cubic fluorite lattice causes a shifting of the ceria peaks toward lower angles indicating the existence of a solid solution. The same result was obtained by Matovic et al. [23].

The crystallite sizes ($D$) were calculated based upon on the (1 1 1) diffraction peak's (main peak's) broadening in the XRD pattern using the Scherrer equation [24–28]:

$$D_{hkl} = \frac{\kappa\lambda}{\beta_{hkl}\cos\theta} \quad (1)$$

where $D_{hkl}$ is the average dimension of the crystallites, $k = 0.9$, $\lambda$ is the wavelength of the X-ray radiation (0.15405 nm), $\theta$ is the Bragg angle for the crystal planes $\{hkl\}$, and $\beta_{hkl}$ is the broadening (full-width at half-maximum (FWHM)) of the peak. Calculated crystallite sizes were 27.6373 nm ($2.76 \times 10^{-8}$ m) and 26.7570 nm ($2.68 \times 10^{-8}$ m) for the sintered powder samples obtained from solution-1 and solution-2, respectively.

Table 2
Calculated lattice parameters for sintered ceramic powder samples.

| Sample | (*hkl*) | 2$\theta$ (°) | FWHM (°) | *d* (Å) | *a* (Å) |
|---|---|---|---|---|---|
| Ce/Nd (a) | (1 1 1) | 28.40 | 0.2965 | 3.1401 | 5.4387 |
| 9/1 | (2 0 0) | 32.95 | 0.3375 | 2.7161 | 5.4322 |
| | (2 2 0) | 47.29 | 0.3495 | 1.9206 | 5.4322 |
| | (3 1 1) | 56.09 | 0.3939 | 1.6383 | 5.4337 |
| | (2 2 2) | 58.75 | 0.4706 | 1.5703 | 5.4398 |
| Ce/Nd (b) | (1 1 1) | 28.17 | 0.3061 | 3.1652 | 5.4822 |
| 7/3 | (2 0 0) | 32.65 | 0.2939 | 2.7404 | 5.4808 |
| | (2 2 0) | 46.92 | 0.3750 | 1.9348 | 5.4725 |
| | (3 1 1) | 55.60 | 0.4386 | 1.6516 | 5.4777 |
| | (2 2 2) | 58.45 | 0.6637 | 1.5777 | 5.4652 |

Table 3
Surface area, pore volume and pore diameter values of the sintered composite powders.

| | BET surface area ($m^2$/g) | Langmure surface area ($m^2$/g) | Pore volume ($cm^3$/g) | Micropore % | Pore size (Å) |
|---|---|---|---|---|---|
| Sample 1 | 9.27 | 17.36 | 0.016 | 43.3 | 70.01 |
| Sample 2 | 6.92 | 13.01 | 0.015 | 38.1 | 90.9 |

The lattice parameters of the samples were determined (see Table 2) by comparing the peak positions (2$\theta$) of the XRD patterns using the below relations [29]:

$$\frac{1}{d^2} = \frac{h^2 + k^2 + l^2}{a^2} \quad (2)$$

Moreover, the dislocation density ($\delta$) is related to the crystallite size ($D$) of the sintered nanoceramic powder as given by

$$\delta = \frac{n}{D^2} \quad (3)$$

where $n$ is a factor ($n = 1$ for minimum dislocation density) [24]. The microstrain ($\varepsilon$) in the nanoceramic powder can be calculated using following equation [24]:

$$\varepsilon = \frac{1}{\tan\theta}\left[\frac{\lambda}{D\cos\theta} - \beta\right] \quad (4)$$

The calculated dislocation densities were $1.3092 \times 10^{11}$ $cm^{-2}$ and $1.3968 \times 10^{11}$ $cm^{-2}$ for the sintered powder samples obtained from solution-1 and solution-2, respectively. The calculated microstrain values were $2.2723 \times 10^{-3}$ and $2.3658 \times 10^{-3}$ for the sintered powder samples obtained from solution-1 and solution-2, respectively.

The nitrogen adsorption measurements of the two sintered powder samples include the determination of (i) the BET and the Langmure surface area, (ii) the volume of pores, and (iii) the pore size. The structural parameters of the sintered powders obtained from the BET analysis were presented in Table 3.

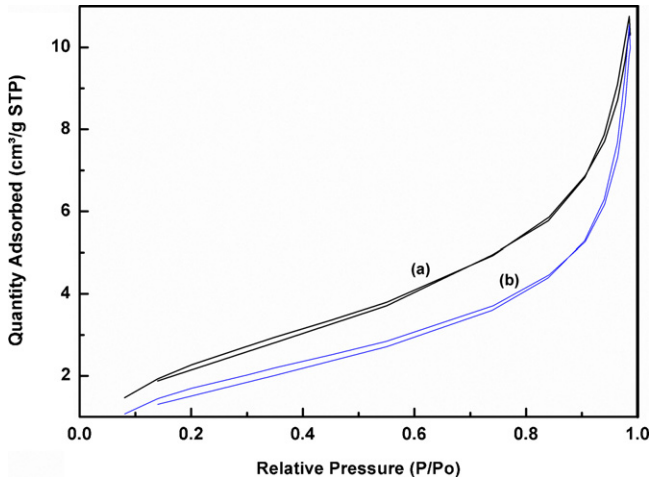


Fig. 5. $N_2$ adsorption/desorption isotherms of the powders prepared from: (a) solution-1, and (b) solution-2.

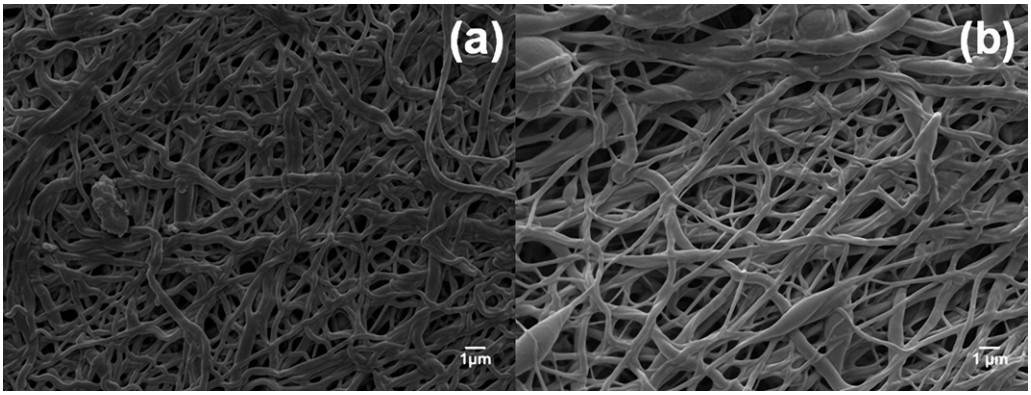


Fig. 6. SEM micrographs of nanofibers electrospun from: (a) solution-1 and (b) solution-2.

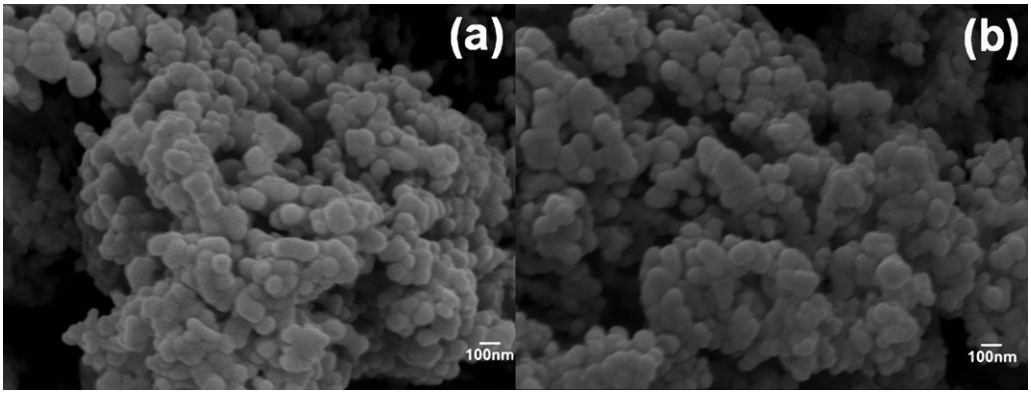


Fig. 7. SEM micrographs of calcined Nd doped ceria composite nanopowders obtained from electrospun nanofibers from: (a) solution-1, and (b) solution-2.

Nd doped ceria of composite powders prepared from the sintering of the calcined powders from the solution-1 exhibits a BET surface area of 9.27 $m^2$/g and and a Langmure surface area of 17.36 $m^2$/g. The Nd acetate content of the polymer solution was increased from 0.1 g to 0.3 g in the preparation of solution-2. As it can be seen from Table 3, the composite sintered powders obtained from the calcination of solution-2 have lower surface areas than the sintered powders prepared from solution-1.

The micropore area is decreasing with the increasing neodymium content of the samples. For sample-1, the micropore area is around 43% of the surface areas and for sample-2, it is around 38%.

Fig. 5 shows the $N_2$ adsorption/desorption isotherms of the sintered powder samples. As it is shown in the isotherm figures of the samples, there are no distinct hysteresis loops at the adsorption/desorption isotherms.

Brunauer et al. [30], found that most of the adsorption isotherms fit into one of the five well-known types given in the literature [31]. Our samples fit into type III groups. Isotherms of this Type are convex to a relative pressure axis and exhibit no limiting adsorption at $P/Po = 1$. Type III isoterms arise when

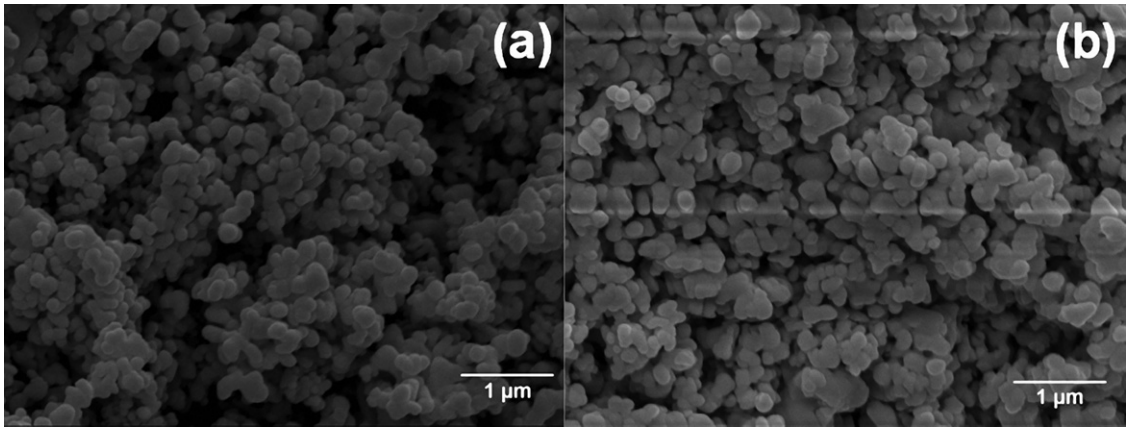


Fig. 8. SEM micrographs of Sintered Nd doped ceria composite nanopowders obtained from electrospun nanofibers from: (a) solution-1, and (b) solution-2.

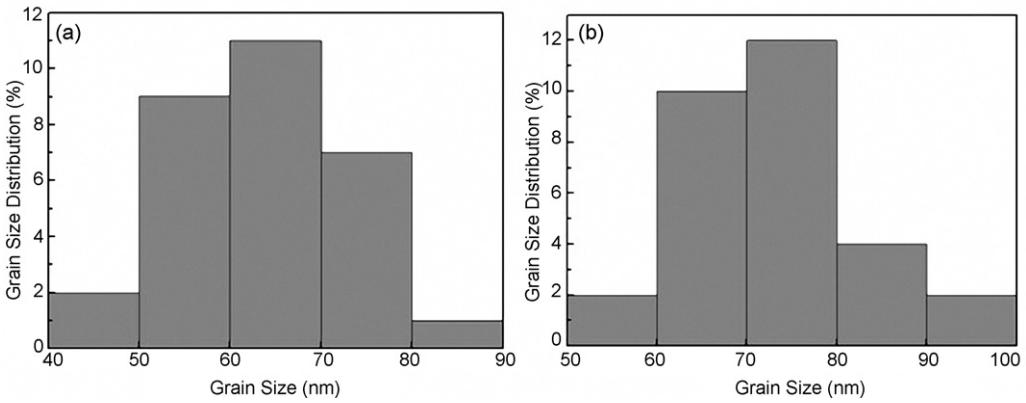


Fig. 9. SEM micrographs of sintered Nd doped ceria composite nanopowders obtained from electrospun nanofibers from: (a) solution-1, and (b) solution-2.

the adsorbate interaction with an adsorbed layer is greater than the interaction with the adsorbent surface.

The SEM analyses were performed to observe the morphology and to determine the fiber diameters of the electrospun hybrid polymer solutions and grain sizes of the calcined and sintered powders. The morphology of the nanofibers electrospun from hybrid polymer solutions 1 and 2 are shown in Fig. 6(a and b). The nanofibers obtained from the electrospinning of the solution-1 are homogeneous with an average diameter of 223 nm and contain no beading. However, the nanofibers obtained from solution-2 are not homogeneous, and their average diameter is 205 nm.

In order to obtain the nanocrystalline ceramic powder sample, the electrospun nanofiber samples were calcined and sintered at 850 °C for 2 h in atmospheric conditions. The SEM micrographs of the calcined and the sintered Nd doped ceria composite nanoceramic powders obtained from the electrospun nanofibers of the hybrid polymer solutions 1 and 2 are shown in Figs. 7 and 8, respectively.

Grain size is very important for the crystal structure because at high operation SOFC temperatures high grain sizes result in cracks. The nano-sized fine-grained oxide structure is advantageous. This is so because the diffusion can easily take place and release the accumulated stresses at high temperatures

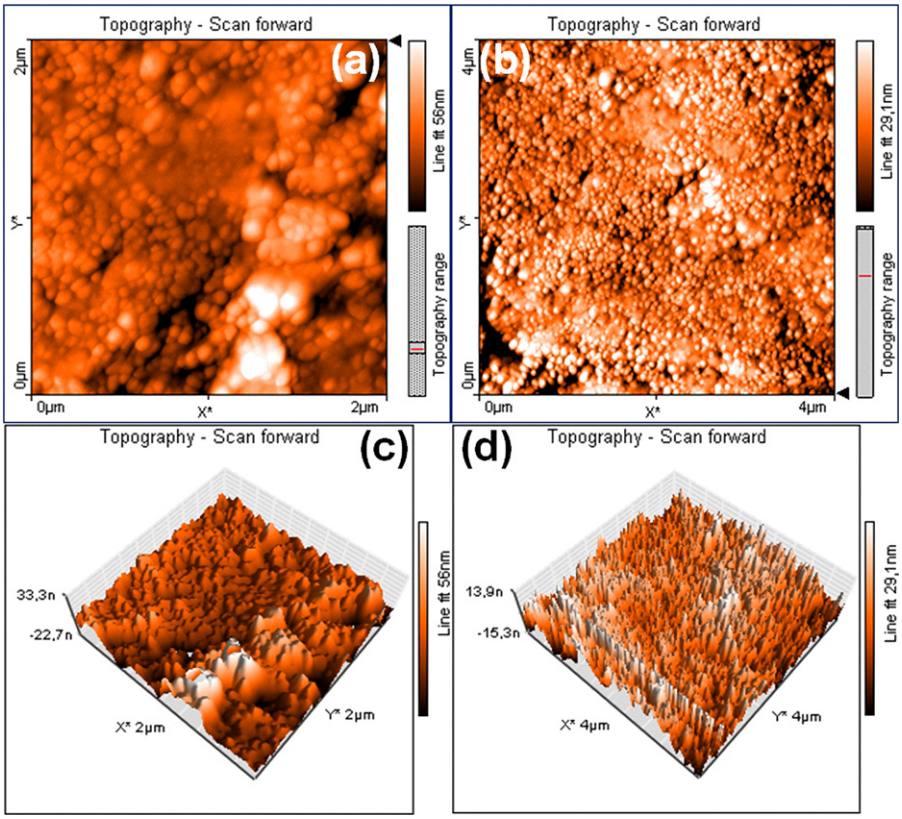


Fig. 10. AFM images of sintered Nd doped ceria composite nanopowders obtained from electrospun nanofibers from solution-1: (a) 2 × 2 μm surface map, (b) 4 × 4 μm surface map, (c) 2 × 2 μm 3D surface map, and (d) 4 × 4 μm 3D surface map.

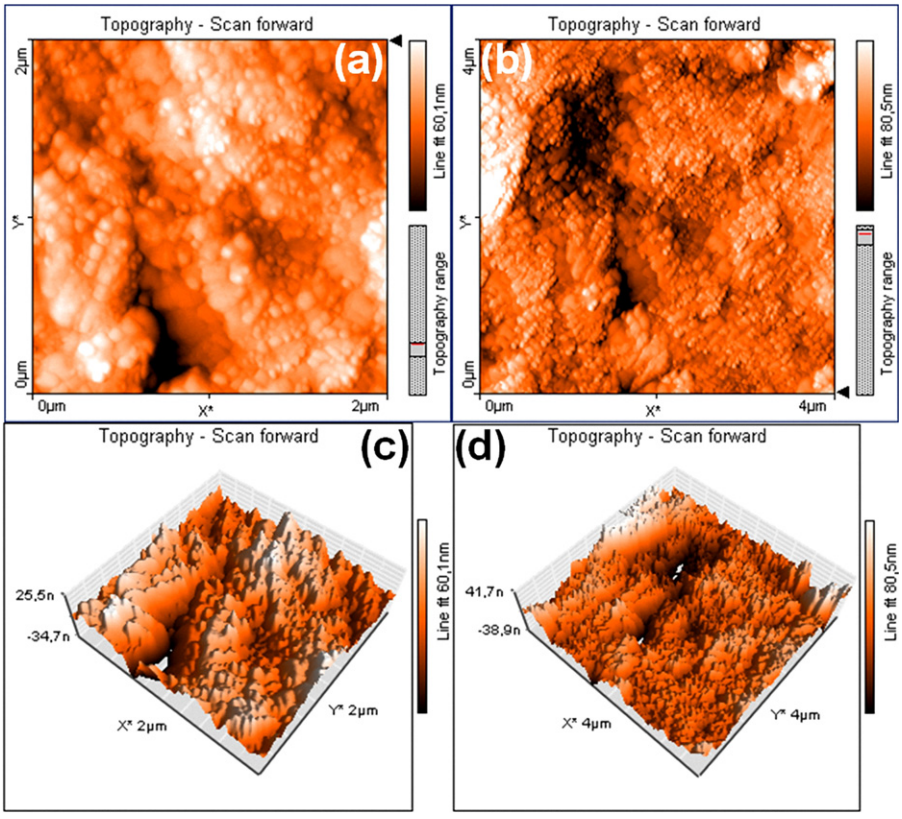


Fig. 11. AFM images of sintered Nd doped ceria composite nanopowders obtained from electrospun nanofibers from solution-2: (a) 2 × 2 μm surface map, (b) 4 × 4 μm surface map, (c) 2 × 2 μm 3D surface map, and (d) 4 × 4 μm 3D surface map.

for large grain sized crystalline ceramic structures [32]. Average grain diameters of the calcined Nd doped ceria composite nanopowders obtained from the solutions 1 and 2 were measured using the ImageJ digital image processing software as 95 nm and 90 nm, respectively. The average grain diameters of the sintered Nd doped ceria nanopowders obtained from the hybrid polymer solutions 1 and 2 were measured as 76 nm and 71 nm, respectively. The grain boundaries are clearly visible for both of the calcined and the sintered powders and the particles are in the form of round agglomerates. The grain size distribution of the sintered powders obtained from solution-1 is very uniform as it can be seen from Fig. 9.

The surface morphology of the sintered nanocrystalline ceramic powder samples was taken using the AFM (intermittent contact mode) to obtain fine details of the nanocrystalline surfaces on a nanoscale. Each measurement contains 512 × 512 data points. Cylindrical pellets of the samples were prepared with an uniaxial cylindrical mold for the measurements. The sintered nanocrystalline ceramic powder samples were pressed into 13 mm diameter pellets under a pressure of 35 MPa.

Fig. 10 displays the surface morphology of the neodymium doped ceria nanocrystalline ceramic powder sample obtained from solution 1. Figs. 10(a and b) are the topographic surface maps of the nanocrystalline ceramic powder sample obtained from solution 1. Spherical grain particles of the nanocrystalline ceramic powder sample can be easily seen from 2 × 2 μm and 4 × 4 μm topographic images. Figs. 10(c and d) are the three-dimensional (3D) surface maps of the sintered nanocrystalline ceramic powder sample obtained from solution-1. The topographic surface maps of the nanocrystalline ceramic powder sample obtained from solution-2 show that the sample has spherical grain, too (see Figs. 11(a and b)). Figs. 11(c and d) are the three-dimensional (3D) surface maps of the sintered

Table 4
Definitions on the surface terminology of surface roughness [33].

| Parameters | Definition | Expression |
|---|---|---|
| $R_a$ (average roughness) | Arithmetic mean of the surface roughness profile from the centerline within the measuring length. | $R_a = \frac{Y1+Y2+\cdots+Yn}{N}$ |
| $R_q$ (root mean square roughness) | Root mean square value of the surface roughness profile from the centerline within the measuring length. | $R_q = \left(\frac{Y1^2+Y2^2+\cdots+Yn^2}{N}\right)^{1/2}$ |
| $R_y$ (peak to valley roughness) | Vertical distance between the highest and lowest points within the overall measuring length. | $R_y = R\max - R\min$ |

Table 5
Surface roughness values for the samples by different definitions.

| Sample | Average roughness ($R_a$) (nm) | Root mean square roughness ($R_q$) (nm) | Peak to valley roughness ($R_y$) (nm) |
|---|---|---|---|
| Sample-1 | 6.4799 | 9.0436 | 80.603 |
| Sample-2 | 8.1091 | 10.388 | 81.616 |

nanocrystalline ceramic powder sample obtained from solution 2. These AFM results are in good agreement with SEM results.

The surface roughness characteristics of the samples were evaluated using intermittent contact mode AFM by different definitions, $R_a$, $R_q$ and $R_y$. The definitions on these terminologies were described by Tak et al. (see Table 4) [33]. The smallest surface roughness values were obtained for the sintered nanocrystalline powder sample obtained from solution-1 (sample-1). According to the surface roughness calculation results based on Table 5, the surface roughness values are 6.4799 nm, 9.0436 nm, and 80.603 nm for average roughness ($R_a$), root mean square roughness ($R_q$), and peak to valley roughness ($R_y$), respectively, for the sintered nanocrystalline powder sample obtained from solution-1 (sample-1). It can be easily seen from Table 5 that the increase in the amount of neodymium and the decrease in the amount of cerium decreased the surface roughness.

## 4. Conclusions

A new method to synthesize Nd doped $CeO_2$ ceramic nanopowders by the electrospinning of the hybrid polymers solution of their composite precursor was put forward. Synthesized ceramic nanopowders were characterized by FT-IR, XRD, BET, SEM, and AFM techniques. The crystallite sizes, lattice parameters, dislocation densities and microstrain values of the samples were calculated. Calculated crystallite sizes were 27.6373 nm ($2.76 \times 10^{-8}$ m) and 26.7570 nm ($2.68 \times 10^{-8}$ m) for the sintered powder samples obtained from solution-1 and solution-2, respectively. The calculated dislocation densities were $1.3092 \times 10^{11}$ cm$^{-2}$ and $1.3968 \times 10^{11}$ cm$^{-2}$ for the sintered powder samples obtained from solution-1 and solution-2, respectively. The calculated microstrain values were $2.2723 \times 10^{-3}$ and $2.3658 \times 10^{-3}$ for the sintered powder samples obtained from solution-1 and solution-2, respectively. BET results show that the increase of the neodymium doped content decrease the surface area of the composite powders. The SEM micrographs show that ultrafine nanocrystalline powders have been obtained by the electrospinning technique. Average grain diameters of the calcined Nd doped ceria composite nanopowders obtained from the solutions 1 and 2 were measured as 95 nm and 90 nm, respectively. According to the surface roughness measurements, the increase in the amount of neodymium and the decrease in the amount of cerium decreased the surface roughness. The smallest surface roughness values were obtained as 6.4799 nm, 9.0436 nm, and 80.603 nm for average roughness ($R_a$), root mean square roughness ($R_q$), and peak to valley roughness ($R_y$), respectively, for the sintered nanocrystalline powder sample obtained from solution-1.

## References


[1] K. Higashi, K. Sonoda, H. Ono, S. Sameshima, Y. Hirata, Synthesis and sintering of rare-earth-doped ceria powder by the oxalate coprecipitation method, J. Mater. Res. 14 (1999) 957–967.
[2] H. Nitani, T. Nakagawa, M. Yamanouchi, T. Osuki, M. Yuya, T.A. Yamamoto, XAFS and XRD study of ceria doped with Pr, Nd or Sm, Mater. Lett. 58 (2004) 2076–2081.
[3] W.Z. Zhu, S.C. Deevi, A review on the status of anode materials for solid oxide fuel cells, Mater. Sci. Eng. A Struct. 362 (2003) 228–239.
[4] S.H. Chan, X.J. Chen, K.A. Khor, A simple bilayer electrolyte model for solid oxide fuel cells, Solid State Ionics 158 (2003) 29–43.
[5] F. Boulc'h, E. Djurado, Structural changes of rare-earth-doped, nanostructured zirconia solid solution, Solid State Ionics 157 (2003) 335–340.
[6] A.B. Stambouli, E. Traversa, Solid oxide fuel cells (SOFCs): a review of an environmentally clean and efficient source of energy, Renew. Sustain. Energy Rev. 6 (2002) 433–455.
[7] K. Huang, J.B. Goodenough, A solid oxide fuel cell based on Sr- and Mg-doped $LaGaO_3$ electrolyte: the role of a rare-earth oxide buffer, J. Alloys Compd. 303 (2000) 454–464.
[8] B.J. Wuensch, K.W. Eberman, C. Heremans, E.M. Ku, P. Onnerud, E.M.Y. Yeo, S.M. Haile, J.K. Stalick, J.D. Jorgensen, Connection between oxygen-ion conductivity of pyrochlore fuel-cell materials and structural change with composition and temperature, Solid State Ionics 129 (2000) 111–133.
[9] A. Aytimur, I. Uslu, S. Kocyigit, F. Ozcan, Magnesia stabilized zirconia doped with boron, ceria and gadolinia, Ceram. Int. (2012) http://dx.doi.org/10.1016/j.ceramint.2012.01.035.
[10] M. Kamiya, E. Shimada, Y. Ikuma, M. Komatsu, H. Haneda, S. Sameshima, Y. Hirata, Oxygen self-diffusion in cerium oxide doped with Nd, J. Mater. Res. 16 (2001) 179–184.
[11] I.E.L. Stephens, J.A. Kilner, Ionic conductivity of $Ce_{1-x}Nd_xO_{2-x/2}$, Solid State Ionics 177 (2006) 669–676.
[12] J.A. Kilner, Fast oxygen transport in acceptor doped oxides, Solid State Ionics 129 (2000) 13–23.
[13] D.Y. Wang, D.S. Park, J. Griffith, A.S. Nowick, Oxygen-ion conductivity and defect interactions in yttria-doped ceria, Solid State Ionics 2 (1981) 95–105.
[14] J. Faber, G. Geoffroy, A. Roux, A. Sylvestre, P. Abélard, A systematic investigation of the dc-electrical conductivity of rare-earth doped ceria, Appl. Phys. A Mater. 49 (1989) 225–232.
[15] L. Aneflous, J.A. Musso, S. Villain, J.R. Gavarri, H. Benyaich, Effects of temperature and Nd composition on non-linear transport properties in substituted $Ce_{1-x}Nd_xO_{2-\delta}$ cerium dioxides, J. Solid State Chem. 177 (2004) 856–865.
[16] S.V. Chavan, P.U.M. Sastry, A.K. Tyagi, Combustion synthesis of nanocrystalline Nd-doped ceria and $Nd_2O_3$ and their fractal behavior as studied by small angle X-ray scattering, J. Alloys Compd. 456 (2008) 51–56.
[17] H. Weller, Colloidal semiconductor q-particles-chemistry in the transition region between solid-state and molecules, Angew. Chem. Int. Ed. Engl. 32 (1993) 41–53.
[18] H. Gleiter, Nanocrystalline solids, J. Appl. Crystallogr. 24 (1991) 79–90.
[19] http://rsbweb.nih.gov/ij/docs/intro.html (last accessed 10.02.12).
[20] R.A. Rocha, E.N.S. Muccillo, Preparation of nanocrystalline gadolinia doped ceria powders by combustion synthesis process, Br. Ceram. Trans. 102 (2003) 216–218.
[21] W. Chen, F. Li, J. Yu, Combustion synthesis and characterization of nanocrystalline $CeO_2$-based powders via ethylene glycol–nitrate process, Mater. Lett. 60 (2006) 57–62.
[22] M.L. Dos Santos, R.C. Lima, C.S. Riccardi, R.L. Tranquilin, P.R. Bueno, J.A. Varela, E. Longo, Preparation and characterization of ceria nanospheres by microwave-hydrothermal method, Mater. Lett. 62 (2008) 4509–4511.
[23] B. Matovic, J. Dukic, A. Devecerski, S. Boskovic, M. Ninic, Z. Dohcevic-Mitrovic, Crystal structure analysis of Nd-doped ceria solid solutions, Sci. Sinter. 40 (2008) 63–68.

[24] B. Karunagaran, R.T.R. Kumar, D. Mangalaraj, S.K. Narayandass, G.M. Rao, Influence of thermal annealing on the composition and structural parameters of DC magnetron sputtered titanium dioxide thin films, Cryst. Res. Technol. 37 (2002) 1285–1292.

[25] P.H. Klug, L.E. Alexander, X-ray Diffraction Procedures for Polycrystalline and Amorphous Materials, Wiley, New York, 1974.

[26] N.S. Prasad, K.B.R. Varma, Nanocrystallization of $SrBi_2Nb_2O_9$ from glasses in the system $Li_2B_4O_7$–SrO–$Bi_2O_3$–$Nb_2O_5$, Mater. Sci. Eng. B 90 (2002) 246–253.

[27] E. Alvarado, L.M. Torres-Martinez, A.F. Fuentes, P. Quintana, Preparation and characterization of MgO powders obtained from different magnesium salts and the mineral dolomite, Polyhedron 19 (2000) 2345–2351.

[28] Y. Ding, G.T. Zhang, H. Wu, B. Hai, L.B. Wang, Y.T. Qian, Nanoscale magnesium hydroxide and magnesium oxide powders: control over size, shape, and structure via hydrothermal synthesis, Chem. Mater. 13 (2001) 435–440.

[29] C. Suryanarayana, M.G. Norton, X-ray Diffraction a Practical Approach, Plenum Press, New York, 1998.

[30] S. Brunauer, L.S. Deming, W.S. Deming, E. Teller, On a theory of the Van der Waals adsorption of gases, J. Am. Chem. Soc. 62 (1940) 1723–1732.

[31] N.U. Yagsi, M.Sc Thesis, Production and characterization of activated carbon from apricot stones, Middle East Technical University, METU, April, 2004.

[32] Z.Y. Liu, W. Gao, K. Dahm, F.H. Wang, The effect of coating grain size on the selective oxidation behaviour of Ni–Cr–Al alloy, Scr. Mater. 37 (1997) 1551–1558.

[33] Y.H. Tak, K.B. Kim, H.G. Park, K.H. Lee, J.R. Lee, Criteria for ITO (indium–tin–oxide) an organic light thin film as the bottom electrode of emitting diode, Thin Solid Films 411 (2002) 12–16.